

DRAFT VERSION FEBRUARY 5, 2026

Typeset using L^AT_EX **manuscript** style in AASTeX7

Cosmic Ray Inter-Station Correlation Variations as Precursors of Geomagnetic Storms: A Statistical Study and Multi-Parameter Early Warning Framework

HAOYANG LI,^{1,*} ZONGYUAN GE,^{1,*} AND ZHAOMING WANG^{1,2,3}

¹*College of Physics and Optoelectronic Engineering, Ocean University of China, Qingdao 266100, China*

²*Engineering Research Center of Advanced Marine Physical Instruments and Equipment of Ministry of Education, Qingdao 266100, China*

³*Qingdao Key Laboratory of Advanced Optoelectronics, Qingdao 266100, China*

ABSTRACT

The modulation of galactic cosmic rays (GCRs) by interplanetary disturbances, manifested as Forbush decreases (FDs), has long been recognized as a signature of coronal mass ejection (CME) passages through the heliosphere. While individual FD events have been extensively studied, systematic investigations of how GCR inter-station correlation variations relate to geomagnetic storm (GS) intensity have not been established. Here we analyze the relationship between GCR characteristics (from a global NM network) and GSs, aiming to understand the physical mechanisms of heliospheric disturbances and to develop complementary predictive capabilities beyond existing L1 solar wind monitoring. By applying a newly introduced anisotropy characteristic method alongside correlation analysis to 25 years of hourly NM data (1995–2020, seven stations), we demonstrate significant correlations between GCR parameters and geomagnetic activity. Inter-station relative differences and anisotropy enhancements show distinct precursor signatures depending on storm intensity, with extreme events displaying detectable signals 48–96 hours in advance. Based on these intensity-dependent response

Corresponding author: Zhaoming Wang

patterns, we propose a “two-stage multi-level” early warning framework: mid-term identification (48–96 hr) triggered by sustained anisotropy increases, followed by short-term grading (0–48 hr) based on inter-station relative difference variations and high-latitude flux changes. Validated on the extreme November 2003 and severe August 2018 geomagnetic storms, our approach successfully identifies precursor signals, providing a potential means to extend GS prediction windows.

Keywords: Sun: coronal mass ejections (CMEs) — Sun: activity — cosmic rays — magnetic fields — methods: statistical

1. INTRODUCTION

Geomagnetic storms (GSs) represent one of the most significant manifestations of space weather, arising from the interaction between solar wind disturbances and Earth’s magnetosphere (W. D. Gonzalez et al. 1994). These events pose substantial risks to technological infrastructure, including satellite operations, power grid stability, and navigation systems (M. N. Pedersen et al. 2024). GSs are driven by two primary solar wind structures: coronal mass ejections (CMEs) and high-speed streams (HSSs) emanating from coronal holes (B. T. Tsurutani et al. 1995; I. G. Richardson & H. V. Cane 2010). CMEs are transient, explosive eruptions that carry massive magnetized plasma structures through interplanetary space (R. Schwenn et al. 2006), typically reaching Earth within 1–5 days depending on their initial speed and propagation conditions (N. Gopalswamy et al. 2001). In contrast, HSSs are quasi-stationary structures that corotate with the Sun, exhibiting characteristic 27-day recurrence patterns; they interact with the preceding slow solar wind to form corotating interaction regions (CIRs) that can also drive geomagnetic activity (B. T. Tsurutani et al. 1995; I. G. Richardson 2018).

The two driver types produce distinct GS characteristics. CME-driven storms tend to be more intense and are responsible for nearly all extreme events ($\text{Dst} < -200 \text{ nT}$), while CIR/HSS-driven

* Co-first author

storms are typically moderate (rarely exceeding $Dst \sim -100$ nT) but more frequent during solar minimum (I. G. Richardson & H. V. Cane 2010; J. Zhang et al. 2007). Crucially, the galactic cosmic ray (GCR) response also differs: CME-associated Forbush decreases (FDs) are generally deeper and more abrupt due to the strong magnetic barriers of CME flux ropes and driven shocks. Specifically, when a CME’s magnetic field contains a strong southward component, magnetic reconnection at the dayside magnetopause efficiently transfers solar wind energy into the magnetosphere, intensifying the ring current and producing characteristic Dst index depressions (W. D. Gonzalez et al. 1994; J. E. Borovsky & J. Birn 2014), while CIR-associated decreases are shallower and more gradual (I. G. Richardson 2004; M. Dumbović et al. 2012). Given that our focus is on developing early warning capabilities for intense GSs—which pose the greatest technological risks—this study concentrates on CME-driven events, where GCR precursor signals are most pronounced.

Current operational space weather forecasting relies on a well-established causal chain: solar eruption observation, interplanetary propagation modeling, and magnetospheric response prediction (H. V. Cane 2000). Coronagraph observations of CMEs can identify potential threats several days in advance, while in-situ solar wind measurements at the first Lagrangian point (L1; e.g., from the Advanced Composition Explorer (ACE) and Deep Space Climate Observatory (DSCOVR) satellites) provide 30–60 minutes of warning before magnetospheric impact (A. V. Belov et al. 1995). Empirical and physics-based models relating solar wind parameters to geomagnetic indices have achieved considerable success (M. Temerin & X. Li 2002; R. Bala & P. Reiff 2012). Recent magnetohydrodynamic (MHD) simulations continue to improve CME propagation fidelity (T. Singh et al. 2025; R. Schwenn et al. 2006). The Space Weather Modeling Framework (SWMF) demonstrates a relatively good predictive skill score for mid-latitude magnetic perturbations (Q. Al Shidi et al. 2022). The deep Gaussian process-based GeoDGP model has further enhanced short-term probabilistic forecasting of ground magnetic perturbations (H. Chen et al. 2025). V. Upendran et al. (2022) developed a fast, global dB/dt forecasting model, which forecasts 30 min into the future using only solar wind measurements as input. However, inherent limitations persist: the L1-to-magnetopause transit time imposes a strict upper bound on warning lead time, CME propagation uncertainties lead to false

alarms or missed detections, and extreme events remain difficult to predict due to sample scarcity (J. W. Bieber & P. Evenson 1998; K. Munakata et al. 2005; H. V. Cane 2000).

Galactic cosmic rays (GCRs) offer a complementary pathway to extend GS prediction windows. As high-energy charged particles (\sim GeV) traversing the heliosphere, GCRs possess large gyroradii and long mean free paths, enabling them to respond rapidly to large-scale interplanetary magnetic field (IMF) structures (A. D. Erlykin & A. W. Wolfendale 2006; J. R. Hörandel 2006). The Forbush decrease (FD)—a sudden, global reduction in GCR intensity accompanying CME passages—has been recognized since S. E. Forbush (1938). The enhanced magnetic field and turbulent structures associated with CME-driven shocks and magnetic clouds scatter and deflect GCRs, producing measurable intensity variations before and during GSs, often accompanied by energetic particle signatures tied to shock acceleration (A. R. Bell 1978; A. V. Belov et al. 2015). Using wavelet transform and cross-correlation analysis of neutron monitor data from KIEL and MOSC stations during 2003–2004, C. Idosa et al. (2023) reported robust negative correlations between cosmic ray flux and Dst.

Beyond isotropic flux changes, GCR anisotropy provides additional diagnostic information. Classical transport theory predicts anisotropic streaming driven by spatial gradients and magnetic field topology (M. A. Forman & L. J. Gleeson 1975; R. Schlickeiser et al. 2019), and early observations reported transient north–south anisotropy during interplanetary disturbances (S. P. Duggal & M. A. Pomerantz 1976). J. W. Bieber & P. Evenson (1998) demonstrated that anisotropy enhancement preceding CME magnetic cloud arrivals originates primarily from $B \times \nabla n$ drift, where density gradients perpendicular to the IMF drive directional particle flows. This mechanism has been confirmed by subsequent studies (J. W. Bieber et al. 1999; K. Munakata et al. 2005). A. V. Belov et al. (1995) identified precursor signals appearing hours to a day before FD onset, attributable to shock acceleration and loss-cone effects. More recently, X. L. Zhu et al. (2015) developed wavelet-based methods detecting 12-hour period enhancements before large storms, while V. G. Grigoryev et al. (2017) reported prediction probabilities of 0.75 using band harmonic analysis of GCR angular distributions. CME-type dependent GCR modulation has also been reported in statistical studies (R. K. Mishra & R. Agarwal 2008).

Recent investigations have further quantified the coupling between solar wind energy and CRI modulation. For instance, [C. I. Uga & B. Adhikari \(2023\)](#) analyzed data from different neutron monitor stations and combined it with solar wind parameters and geomagnetic indices, confirming in a study spanning multiple observational cycles that variations in cosmic ray intensity (CRI) not only respond to global solar-terrestrial disturbances but also exhibit significant spatial variation characteristics across stations. [C. I. Uga et al. \(2025\)](#) employed Superposed Epoch Analysis and Wavelet Transform Coherence to demonstrate a strong inverse correlation between CRI and key coupling parameters during intense storms, with the coherence being most pronounced during super-storm events. This underscores the importance of storm intensity and solar wind drivers in shaping GCR responses, yet an integrated early-warning framework utilizing multiple GCR characteristics remains undeveloped.

Despite these advances, several gaps remain. First, many key results derive from case studies rather than systematic large-sample statistical analyses, making it difficult to quantify precursor signal universality and stability ([A. V. Belov et al. 1995](#); [K. Munakata et al. 2005](#)). Second, anisotropy quantification methods vary widely, from complex spherical harmonic inversions to qualitative multi-station comparisons, hindering operational implementation ([J. W. Bieber & P. Evenson 1998](#); [R. Schlickeiser et al. 2019](#)). Third, integrated frameworks combining multiple GCR characteristics for graded warnings across different storm intensities have not been developed ([V. G. Grigoryev et al. 2017](#); [X. L. Zhu et al. 2015](#)).

This paper addresses these limitations through systematic analysis of 25 years of neutron monitor (NM) data spanning 2809 GS events. We quantify correlations between GCR flux, inter-station relative differences, and anisotropy with GS intensity. We introduce a simplified anisotropy characteristic method suitable for real-time monitoring. Based on the distinct response patterns observed for different storm intensities, we construct an integrated “two-stage multi-level” early warning framework and validate it against representative extreme and severe storm events.

2. DATA AND METHODS

2.1. *Observational Data*

We utilize hourly pressure-corrected count rates from seven NM stations in the Neutron Monitor Database (NMDB; <http://www.nmdb.eu>): OULU (Finland, 65.1°N), JUNG (Jungfraujoch, Switzerland, 46.5°N), SOPO (South Pole, 90.0°S), THUL (Thule, Greenland, 76.5°N), KERG (Kerguelen, 49.4°S), PTFM (Potchefstroom, South Africa, 26.7°S), and TSMB (Tsumeb, Namibia, 19.2°S). NM response characteristics and rigidity dependence are described in J. M. Clem & L. I. Dorman (2000). This network provides global coverage spanning both hemispheres and multiple longitude sectors, essential for anisotropy characterization. The study period extends from 1995 January to 2020 December, encompassing solar cycles 23 and 24.

Geomagnetic activity is characterized using the hourly Dst index from the World Data Center for Geomagnetism, Kyoto. Storms are classified into four intensity levels based on minimum Dst: minor ($-50 < \text{Dst}_{\min} \leq -30$ nT; 1975 events), moderate ($-100 < \text{Dst}_{\min} \leq -50$ nT; 711 events), severe ($-200 < \text{Dst}_{\min} \leq -100$ nT; 107 events), and extreme ($\text{Dst}_{\min} \leq -200$ nT; 16 events). The total dataset comprises 280,808 hourly data points.

Data preprocessing includes: (1) outlier removal using the 3σ criterion; (2) linear interpolation for isolated missing values; and (3) temporal alignment across all data sources. Quiet periods are defined as intervals where Dst remains between -30 and $+30$ nT for at least 12 consecutive hours, occurring more than 100 hours before storm peak times to exclude pre-storm disturbance contamination. Station flux baselines are computed as mean count rates during all identified quiet periods.

2.2. *Analysis Framework*

Our analysis proceeds in three stages, addressing the two key questions: (1) How do GCR characteristics correlate with GS intensity? and (2) Can these correlations provide early warning signals?

Stage 1: Correlation analysis. We first establish the statistical relationship between GCR parameters (flux, inter-station differences) and Dst using Pearson (r_p) and Spearman (r_s) correlation coefficients. Time-lag analysis identifies optimal warning lead times by computing correlations for

lags from -48 to $+48$ hours, where positive lags indicate GCR variations preceding geomagnetic response.

Stage 2: Anisotropy assessment. We evaluate whether spatial non-uniformity in GCR flux (anisotropy) provides earlier precursor signals than isotropic flux changes. Two methods are employed: the established spherical harmonic analysis and a simplified anisotropy characteristic method introduced here for operational applications.

Stage 3: Case validation. Representative extreme and severe storm events are analyzed to verify that the statistically identified precursor patterns manifest in individual cases.

2.3. *GCR Characteristic Parameters*

We define two key parameters to characterize GCR variations:

Inter-station relative difference (δ). To capture asymmetric GCR modulation, we compute:

$$\delta = CR_{\text{OULU}} \times K - CR_{\text{JUNG}} \quad (1)$$

where $K = \bar{CR}_{\text{JUNG}} / \bar{CR}_{\text{OULU}}$ is the ratio of quiet-period mean fluxes. This normalization removes systematic differences between stations, isolating differential modulation effects. The OULU–JUNG baseline (65°N to 46°N) provides sensitivity to north–south asymmetries induced by CME magnetic structures.

Anisotropy characteristic (A_{basic}). We introduce a simplified metric for operational monitoring:

$$A_{\text{basic}}(t) = \sum_{i=1}^7 R_i(t)^2 \quad (2)$$

where $R_i(t)$ is the relative count rate deviation from the quiet-period baseline at station i . This quantity represents the total variance across the station network, increasing when flux variations become spatially non-uniform. Unlike traditional spherical harmonic analysis (J. W. Bieber & P. Evenson 1998), which requires complex fitting procedures, A_{basic} can be computed in real-time from raw NM data.

For comparison, we also compute the $B \times \nabla n$ drift anisotropy using spherical harmonic expansion following J. W. Bieber & P. Evenson (1998). Anisotropy enhancement is quantified as the percentage

change relative to quiet-period values, with statistical significance assessed using Welch's t-test ($p < 0.05$, $p < 0.01$, $p < 0.001$).

3. RESULTS

Our results are organized around three questions: (1) How strongly do GCR parameters correlate with GS intensity? (2) Can GCR anisotropy provide earlier warning than flux variations alone? (3) Do these patterns hold in individual storm events?

3.1. *GCR–Geomagnetic Storm Correlations*

3.1.1. *Overall Correlation Patterns*

Table 1 presents correlation coefficients between GCR parameters and the Dst index for different storm intensities. All parameters exhibit statistically significant correlations ($p < 0.001$), with three key patterns:

First, *intensity dependence*: Correlation coefficients systematically increase with storm intensity. For OULU flux, Spearman coefficients increase from 0.268 (minor storms) to 0.466 (extreme storms), reflecting stronger GCR modulation by more energetic CME-driven disturbances.

Second, *parameter robustness*: The inter-station relative difference δ maintains consistently strong negative correlations across all intensity levels ($|r_s| = 0.385\text{--}0.405$), outperforming single-station measurements. This stability arises because δ removes common-mode variations (e.g., pressure effects), amplifying the differential signal from asymmetric CME modulation.

Third, *latitude dependence*: High-latitude stations (OULU, THUL, SOPO) show stronger correlations than low-latitude stations (TSMB, PTFM), consistent with lower cutoff rigidities and enhanced GCR modulation sensitivity.

3.1.2. *Temporal Characteristics and Warning Lead Times*

Time-lag analysis reveals intensity-dependent temporal relationships (Table 2 and Figure 1). For minor and moderate storms, GCR flux changes lead the Dst index by 9–17 hours, providing valuable early warning windows. This lead time corresponds to the gradual energy transfer process as CME-driven disturbances propagate toward Earth.

Table 1. Correlation Coefficients Between GCR Parameters and Dst Index

Storm Level	OULU Flux		Relative Diff. (δ)	
	r_s	r_p	r_s	r_p
Minor	0.268	0.300	-0.385	-0.360
Moderate	0.342	0.352	-0.405	-0.417
Severe	0.397	0.370	-0.402	-0.447
Extreme	0.466	0.425	-0.389	-0.394

NOTE—All correlations significant at $p < 0.001$. Sample sizes: Minor (197,408), Moderate (71,100), Severe (10,700), Extreme (1,600).

In contrast, severe and extreme storms exhibit near-zero optimal lag times, indicating that GCR flux variations and Dst decline occur nearly simultaneously. This synchronicity reflects rapid physical processes during intense events: under extreme solar wind energy injection, ring current enhancement and magnetospheric restructuring represent two simultaneous consequences of the same impulsive forcing.

The temporal evolution of correlations (Figure 1) shows distinct patterns. For severe storms, the relative difference δ achieves its maximum correlation ($r_s = -0.568$) in the 0–20 hour window, demonstrating exceptional short-term warning capability. For extreme storms, OULU flux correlation reaches $r_s = 0.585$ in the 0–20 hour window, the highest among all parameter-intensity combinations.

Analysis across multiple time windows (6–48 hours; Figure 2) confirms that GCR modulation operates over timescales of hours to days, with cumulative effects better captured in extended observation windows. The δ mean under 24-hour windows correlates most strongly with Dst mean ($r_s = -0.423$), suggesting that sustained asymmetric modulation approximately one day before storm onset provides reliable warning signals.

3.2. Anisotropy Enhancement as Early Warning Indicator

Can GCR anisotropy provide earlier warning than flux variations alone? Tables 3 and 4 present results from spherical harmonic analysis and our simplified anisotropy characteristic method, respectively.

Table 2. Optimal Lag Times for Different Storm Intensities

Storm Level	Station	Max $ r $	Lag (hr)
Minor	JUNG	0.221	16
	TSMB	0.230	17
Moderate	JUNG	0.281	9
	PTFM	0.289	16
Severe	JUNG	0.311	0
	TSMB	0.292	0
Extreme	OULU	0.466	0
	THUL	0.495	0

Key finding: GCR anisotropy shows statistically significant enhancement 48–96 hours before extreme storms—substantially earlier than the near-zero lag times found for flux correlations. This extended lead time makes anisotropy particularly valuable for early warning.

For severe storms, the $B \times \nabla n$ drift anisotropy (from spherical harmonic analysis) increases by +50.2% in the 0–24 hour window ($p < 0.001$). For extreme storms, our simplified A_{basic} metric shows +47.5% enhancement even 72–96 hours before the event ($p < 0.001$).

Enhancement amplitude correlates positively with storm intensity: minor/moderate storms show modest enhancements (7–40%), while severe/extreme storms produce substantially larger signals (50–138%). Importantly, the simplified A_{basic} method yields results consistent with traditional spherical harmonic analysis, validating its use for operational applications.

3.3. Case Validation

Do the statistically identified patterns manifest in individual storm events? We examine two representative cases: the 2003 November extreme storm and the 2018 August severe storm.

3.3.1. 2003 November 20 Extreme Storm

The extreme GS of 2003 November 20 ($\text{Dst}_{\min} = -422$ nT), associated with the intense solar activity of solar cycle 23, provides an ideal test case (Figure 3). During the 20 hours preceding the

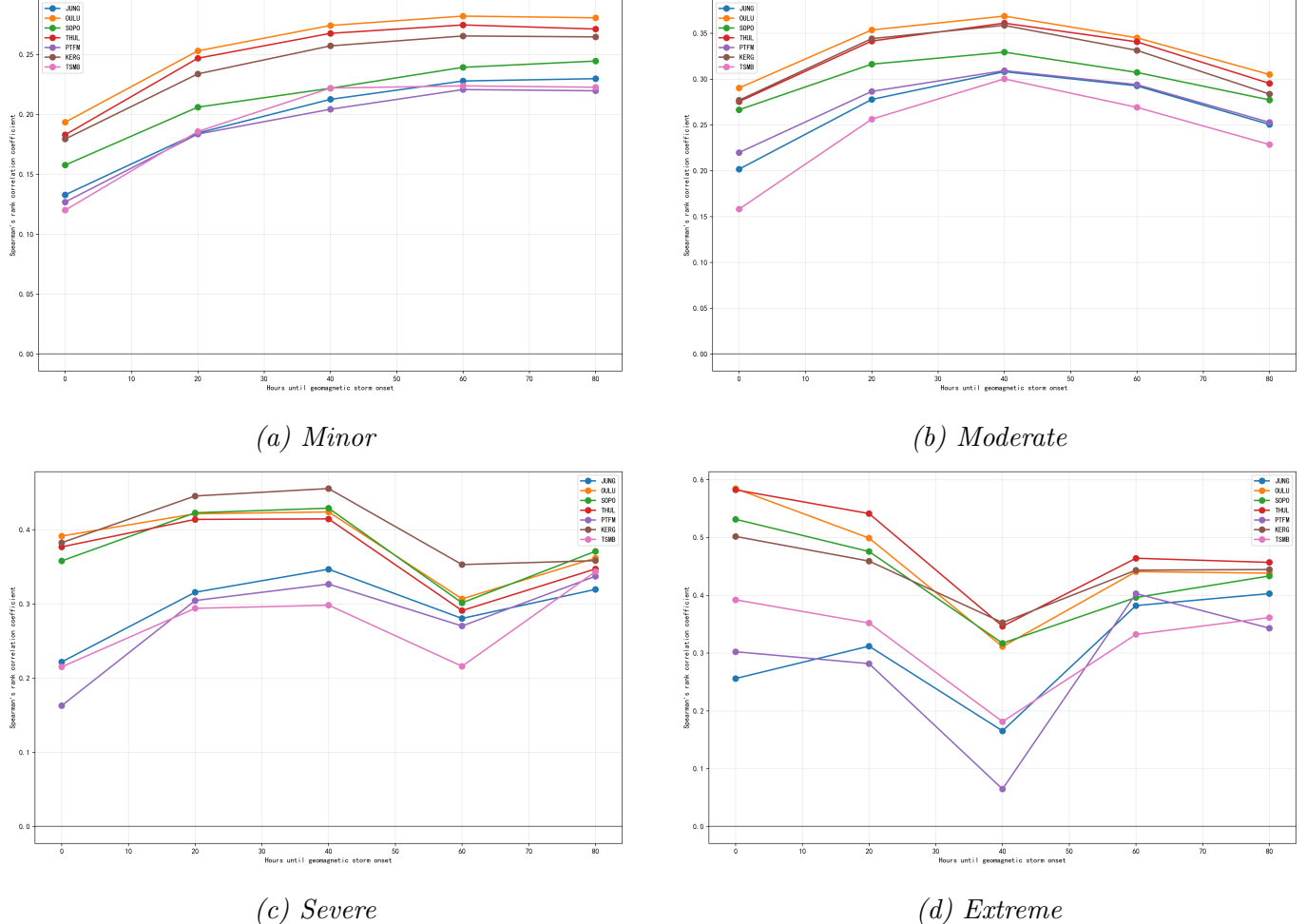


Figure 1. Temporal evolution of Spearman correlation coefficients between GCR parameters and Dst index across five consecutive 20-hour segments before storm peak for (a) minor, (b) moderate, (c) severe, and (d) extreme storms. Each panel shows correlations for individual station fluxes and the inter-station relative difference δ . Higher absolute values indicate stronger predictive capability. Note the distinct temporal patterns: δ peaks at 0–20 hours for severe storms ($r_s = -0.568$), while extreme storms show the strongest flux correlations in the same window.

storm main phase, all stations exhibited flux values below their quiet-period baselines, indicating global GCR suppression consistent with CME-driven FD onset.

Approximately 10 hours before the storm, all stations showed synchronized further flux decreases, reflecting enhanced modulation as the CME structure approached Earth. However, as the main phase began (rapid Dst decline), station responses diverged markedly: low-latitude stations (TSMB, PTFM, JUNG) showed flux recovery, while high-latitude stations continued declining. This spatially

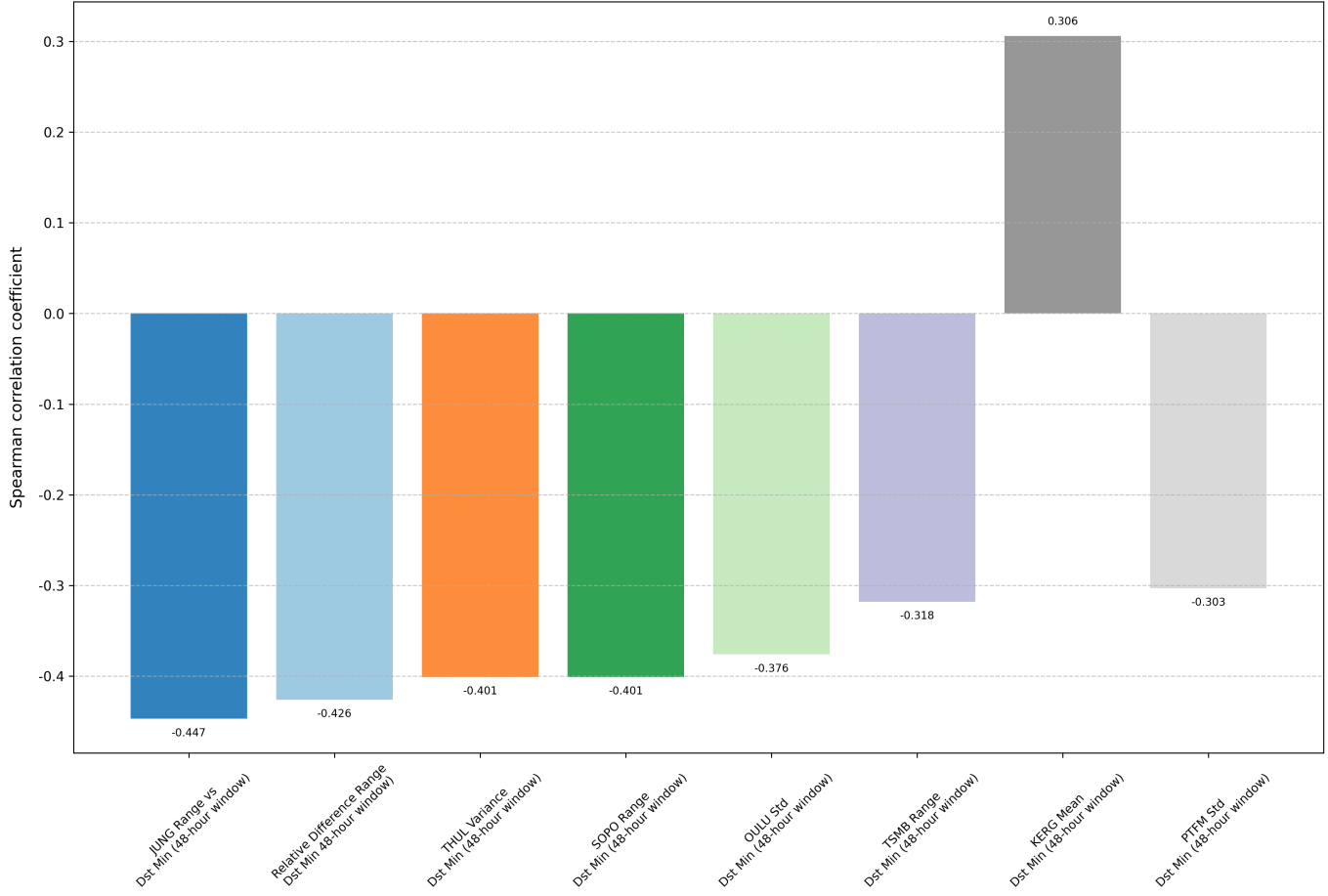


Figure 2. Spearman correlation coefficients between GCR parameter statistics (mean, standard deviation, range) and Dst statistics across different time windows (6, 12, 24, 48 hours). The δ parameter demonstrates consistently strong negative correlations across all window lengths, supporting its utility as a robust warning indicator.

dependent differential response produced pronounced inter-station relative difference (δ) variations and anisotropy enhancement.

The divergent behavior likely originates from asymmetric modulation by the CME magnetic flux rope structure at different geomagnetic latitudes. Low-latitude regions may experience brief signal enhancements due to energetic particle precipitation along open field lines or equatorial penetration mechanisms, while high-latitude regions remain in strong suppression. This spatial heterogeneity—

Table 3. Anisotropy Enhancement (%): Spherical Harmonic Analysis

Level	Window	Total	$B \times \nabla n$	Transverse
Minor	0–24h	+11.1***	+11.5***	+11.3***
	72–96h	+8.7***	+6.7***	+9.0***
Moderate	0–24h	+10.5***	+14.0***	+10.6***
	72–96h	+9.7***	+11.4***	+9.8***
Severe	0–24h	+27.7***	+50.2***	+27.9***
	72–96h	+13.0***	+13.3***	+13.2***
Extreme	0–24h	+33.6***	+44.1***	+34.3***
	72–96h	+12.1**	-0.03	+12.7***

NOTE—Significance levels: * $p < 0.05$, ** $p < 0.01$, *** $p < 0.001$. Only 0–24h and 72–96h windows shown; full results available in supplementary material.

Table 4. Anisotropy Enhancement (%): Simplified A_{basic} Method

Level	Window	A_{basic}	A_{weight}
Minor	0–24h	+61.6**	+63.5**
	72–96h	+30.9***	+30.3***
Moderate	0–24h	+26.4	+26.4
	72–96h	+18.3***	+18.7***
Severe	0–24h	+81.7***	+80.8***
	72–96h	+46.3***	+45.5***
Extreme	0–24h	+138.2***	+131.2***
	72–96h	+47.5***	+46.5***

NOTE—Significance levels: * $p < 0.05$, ** $p < 0.01$, *** $p < 0.001$. Direction-weighted A_{weight} shows marginal differences from basic A_{basic} , suggesting the simpler metric suffices for operational use.

the essence of GCR anisotropy—was effectively captured by both spherical harmonic analysis and the anisotropy characteristic method.

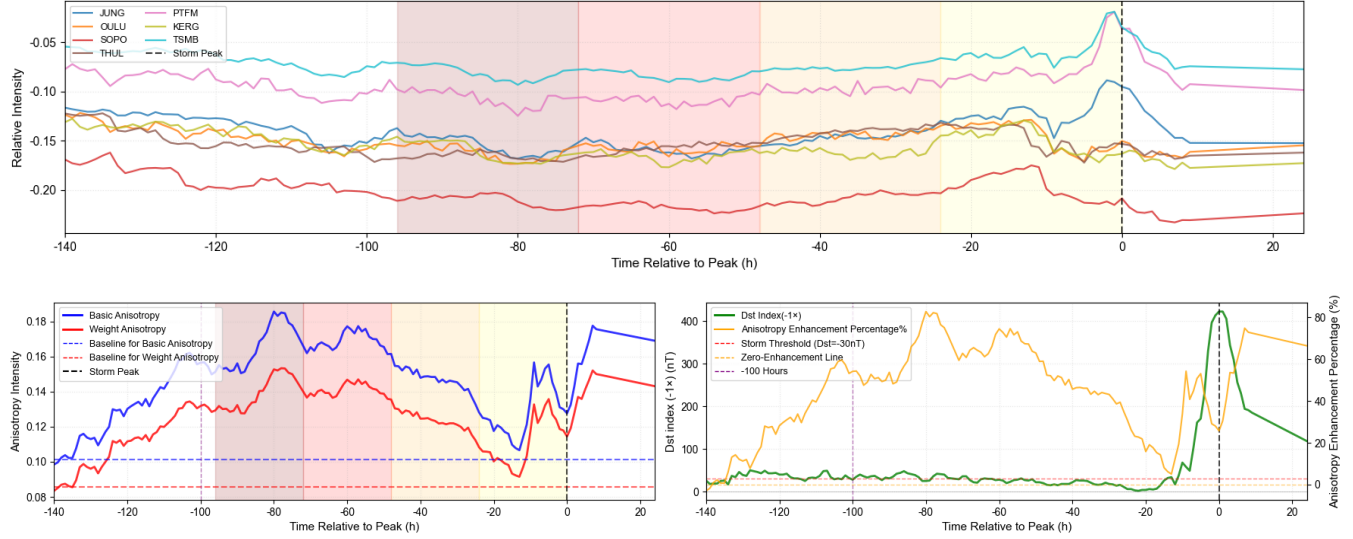


Figure 3. Cosmic ray variations during the 2003 November 20 extreme geomagnetic storm ($Dst_{min} = -422$ nT). *Top panel:* Time series of relative cosmic ray flux deviations from quiet-period baselines for all seven neutron monitor stations (OULU, JUNG, SOPO, THUL, KERG, PTFM, TSMB). Each colored curve represents a different station, showing the temporal evolution of flux variations during the 100-hour period surrounding the storm. Note the initial synchronized decrease followed by spatially divergent responses as the storm main phase develops. *Bottom panel:* Comparison between the basic anisotropy characteristic A_{basic} (red curve, left axis) and the Dst index (blue curve, right axis, sign reversed for visualization). The vertical dashed line marks the storm peak time (minimum Dst). The pronounced anisotropy enhancement preceding and during the main phase demonstrates the method’s sensitivity to approaching CME structures.

3.3.2. 2018 August 26 Severe Storm

The 2018 August 26 severe storm ($Dst_{min} = -176$ nT) exhibits more complex spatiotemporal evolution (Figure 4). During 40–80 hours before the storm, significant non-synchronous flux variations appeared across stations, with some rising and others falling. Although the Dst index had not yet entered its main phase, the anisotropy characteristic method sensitively captured these early disturbance signals.

Approximately 20 hours before the storm, station responses converged toward uniform decreases, entering a typical “global suppression” phase corresponding to the CME main structure arrival. This transition from directional modulation (anisotropy enhancement) to global suppression (isotropic de-

crease) at different storm development stages supports the rationale for a two-stage warning framework: mid-term identification through anisotropy signals (48–96 hours), followed by short-term intensity grading through flux variation analysis (0–48 hours).

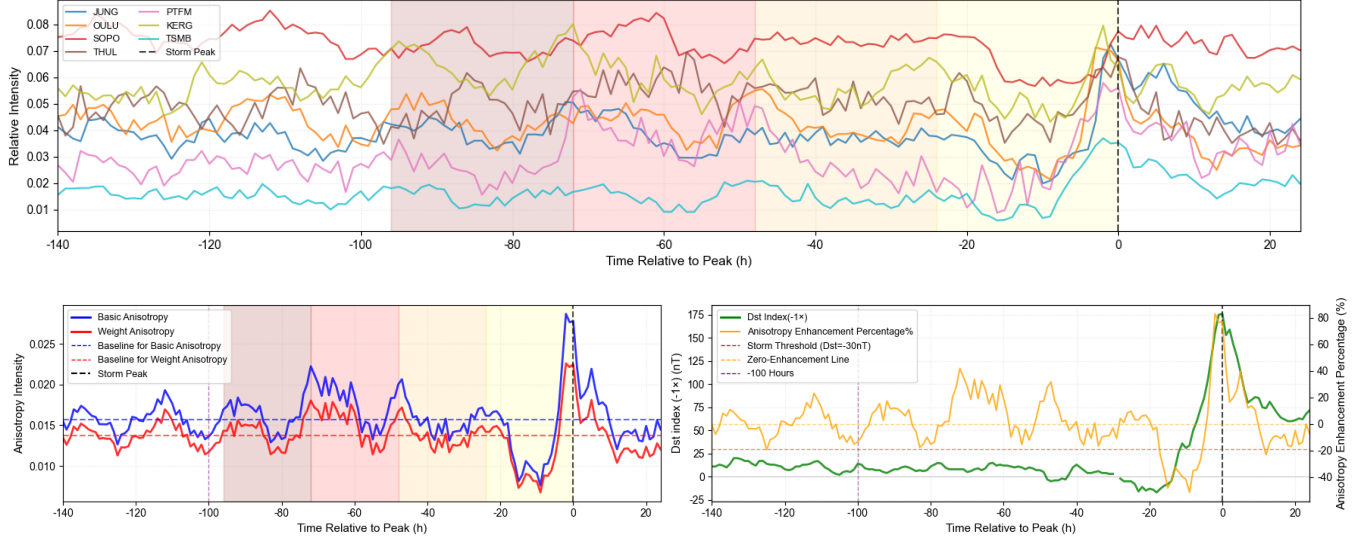


Figure 4. Cosmic ray variations during the 2018 August 26 severe geomagnetic storm ($Dst_{min} = -176$ nT). *Top panel:* Time series of relative cosmic ray flux deviations from quiet-period baselines for all seven neutron monitor stations. Unlike the 2003 extreme event, this storm exhibits more complex spatiotemporal evolution with non-synchronous flux variations appearing 40–80 hours before the storm, followed by convergence toward uniform decreases approximately 20 hours before the peak. *Bottom panel:* Basic anisotropy characteristic A_{basic} (red) and Dst index (blue, sign reversed). The anisotropy shows elevated values during the early non-synchronous phase (indicating directional modulation) before the global suppression phase begins. This two-phase pattern supports the rationale for a two-stage warning framework combining mid-term anisotropy monitoring with short-term flux analysis.

4. DISCUSSION

4.1. Physical Interpretation

The observed correlations between GCR characteristics and GSs reflect the shared CME driver. CMEs and their driven shocks modulate GCRs through magnetic field enhancement and turbulent scattering, while simultaneously transferring energy to Earth's magnetosphere through magnetic re-

connection (H. V. Cane 2000; W. D. Gonzalez et al. 1994; R. Schwenn et al. 2006). The correlation gradient with storm intensity arises because more energetic CMEs produce both stronger GCR modulation and more intense geomagnetic disturbances (R. K. Mishra & R. Agarwal 2008).

The distinct time-lag patterns for different storm intensities reveal underlying physical mechanisms. Minor and moderate storms, often associated with slower CME propagation or weaker driving, show 9–17 hour lead times reflecting gradual solar wind–magnetosphere energy coupling (M. Temerin & X. Li 2002; R. Bala & P. Reiff 2012). Severe and extreme storms, driven by fast, powerful CMEs, exhibit near-synchronous GCR and Dst responses because the rapid magnetospheric reconfiguration and GCR modulation represent two simultaneous manifestations of impulsive energy injection (J. W. Bieber & P. Evenson 1998; K. Munakata et al. 2005).

The exceptional sensitivity of $B \times \nabla n$ drift anisotropy to approaching storms aligns with theoretical expectations. As a CME magnetic structure approaches, it creates a GCR density gradient perpendicular to the IMF. Particle drift along this gradient produces enhanced anisotropy detectable 48–96 hours in advance, when the CME is still beyond 1 AU but its extended magnetic structure already influences GCR propagation (J. W. Bieber & P. Evenson 1998; M. A. Forman & L. J. Gleeson 1975; K. Munakata et al. 2005).

4.2. *Two-Stage Multi-Level Early Warning Framework*

Based on our findings, we propose an integrated early warning framework combining mid-term identification with short-term intensity grading:

Stage 1: Precursor Identification (48–96 hours before storm)—Continuous monitoring of anisotropy parameters using either spherical harmonic analysis or the anisotropy characteristic method. When total anisotropy or $B \times \nabla n$ drift components show sustained increases exceeding 2σ of the quiet-period background across consecutive 6-hour sliding windows, a precursor warning is triggered. This stage provides advance notice that an interplanetary disturbance capable of producing a GS is approaching, enabling preparation of protective measures for critical infrastructure.

Stage 2: Intensity Grading (0–48 hours before storm)—Integration of flux variation rates and inter-station relative difference (δ) for storm intensity classification. For potential severe storms,

rapid negative jumps in δ within 0–20 hours trigger warning upgrades. For extreme events, emphasis is placed on sustained high-latitude station flux decreases combined with rapid anisotropy enhancement. For minor and moderate storms, extended time windows (40–80 hours) are used to analyze cumulative flux variations, ensuring warning coverage while reducing missed detections.

Warning decisions follow a multi-parameter consistency principle: warning triggers or upgrades require synchronized evolution of at least two independent characteristics (e.g., anisotropy enhancement and δ variation), substantially reducing false alarm rates from single-indicator variability.

For operational integration, the framework can be implemented as a continuously updating scoring system that combines normalized anomaly levels of anisotropy and inter-station differences, with decision thresholds calibrated by storm intensity class. This allows flexible tuning between missed-event risk and false-alarm tolerance while preserving physical interpretability. In practice, the GCR-based module is intended to complement L1 solar wind monitoring by extending the lead time of actionable alerts rather than replacing established forecasting chains.

4.3. *Physical Basis for Time Window Selection*

The 100-hour (approximately 4-day) analysis window employed in this study is grounded in well-established CME propagation physics. Fast CMEs with initial speeds exceeding 1000 km s^{-1} typically reach Earth within 1–2 days, while slower CMEs ($\sim 400\text{--}600 \text{ km s}^{-1}$) or those with significant deflection from the Sun-Earth line may require 4–5 days (N. Gopalswamy et al. 2001; P. K. Manoharan et al. 2004). Statistical analyses of large CME samples indicate a median Sun-to-Earth transit time of approximately 80 hours, with the distribution spanning 20–120 hours depending on initial speed and interplanetary conditions (N. Gopalswamy et al. 2001; B. Vršnak et al. 2013).

For GCR-based early warning, the relevant timescale is not the total CME transit time but rather when the CME’s extended magnetic structure begins modulating GCR fluxes detectable at Earth. The magnetic field enhancement and turbulent sheath region ahead of the CME ejecta can influence GCR propagation paths even before the CME main body arrives, producing anisotropy signatures 48–96 hours in advance—consistent with our statistical findings. The 100-hour window thus encom-

passes the full range of physically plausible precursor intervals while minimizing contamination from unrelated solar activity.

We note that CIR/HSS-driven disturbances follow different timescales: the high-speed stream typically reaches Earth approximately 3 days after the associated coronal hole crosses central meridian (B. Vršnak et al. 2007). However, as discussed in Section 1, CIR-associated GCR modulation is weaker and more gradual, making these events less suitable for GCR-based early warning. Our framework is therefore optimized for CME-driven storms, which dominate the severe and extreme categories of greatest concern for space weather operations.

4.4. *Implications for Operational Warning Strategies*

Our results reveal distinct precursor characteristics for different storm intensity levels, suggesting that operational warning strategies should adopt intensity-dependent approaches. For severe and extreme storms ($Dst < -100$ nT), anisotropy enhancement provides robust precursor signals 48–96 hours in advance, enabling mid-term warnings that can inform decisions about satellite operations, power grid configurations, and aviation routing. The near-synchronous GCR-Dst relationship during these events reflects the impulsive nature of intense CME-magnetosphere coupling, where multiple signatures emerge simultaneously rather than sequentially.

For minor and moderate storms, the 9–17 hour lead times identified through time-lag analysis, while shorter, still provide operationally useful warning windows. The graded response pattern—where precursor lead times and correlation strengths scale with storm intensity—supports a tiered alert system. Initial alerts based on anisotropy thresholds can be refined as events develop, with intensity estimates updated using inter-station relative differences and flux variation rates in the hours preceding expected impact.

The multi-parameter consistency requirement (Section 4.2) addresses the practical challenge of balancing false alarm rates against missed detections. In operational contexts, false alarms carry economic costs (unnecessary protective actions), while missed detections risk infrastructure damage. Our framework’s requirement for corroborating signals from multiple independent GCR characteris-

tics provides a mechanism for tuning this trade-off based on user risk tolerance and specific application requirements.

4.5. *Limitations and Future Directions*

Several aspects merit continued development. The current NM network exhibits spatial asymmetry, with concentration at mid-latitudes and sparse coverage in polar regions and at the equator. This non-uniform distribution may introduce systematic biases in spherical harmonic anisotropy reconstruction, particularly for higher-order moments. Future expansion of the monitoring network, especially in polar regions, would improve spatial coverage.

The simplified anisotropy characteristic method, while operationally convenient, captures only the total variance in station responses without distinguishing directional components. More sophisticated algorithms incorporating real-time solar wind parameters and geomagnetic field models could enhance physical interpretability and predictive accuracy.

Our analysis establishes statistical correlations that form the foundation for predictive capability. The natural progression from statistical characterization to operational forecasting involves systematic validation against independent event catalogs and real-time testing over extended periods. Such validation efforts, while beyond the scope of this initial study, represent essential next steps toward operational implementation.

Finally, extreme events remain challenging due to sample scarcity. Our dataset contains only 16 extreme storms, limiting statistical confidence for this most consequential category. Retrospective analysis of historical extreme events (e.g., the 1989 March storm) and continued data accumulation will strengthen predictions for rare but impactful events.

5. CONCLUSIONS

We have conducted a systematic statistical analysis of GCR characteristics and GSs using 25 years of global NM data spanning 2809 events. Our principal findings demonstrate that GCR flux and inter-station relative difference show significant correlations with GS intensity ($p < 0.001$), with correlation coefficients increasing systematically from minor to extreme storms. The relative

difference parameter achieves optimal warning capability ($r_s = -0.568$) in the 0–20 hours before severe storms, outperforming single-station measurements by removing common-mode variations and amplifying differential signals from asymmetric CME modulation.

GCR anisotropy exhibits substantial enhancement 48–96 hours before extreme storms, providing substantially earlier warning signals than flux variations alone. The $B \times \nabla n$ drift anisotropy, derived from spherical harmonic analysis, increases by +50% before severe storms, while the basic anisotropy characteristic shows +47% enhancement 72–96 hours before extreme events. Time-lag analysis reveals intensity-dependent response patterns: minor/moderate storms show 9–17 hour lead times, while severe/extreme storms exhibit near-synchronous GCR and Dst variations, reflecting different energy transfer dynamics between gradual solar wind–magnetosphere coupling and impulsive energy injection processes.

Case studies of the 2003 November extreme storm and 2018 August severe storm validate that anisotropy enhancement and inter-station differential responses serve as identifiable precursor signals, captured effectively by both spherical harmonic analysis and our simplified anisotropy characteristic method. These results support the development of an integrated “two-stage multi-level” early warning system combining mid-term anisotropy monitoring (48–96 hours) with short-term flux analysis (0–48 hours). Such a system could substantially extend GS prediction windows beyond current L1 monitoring capabilities, providing valuable preparation time for protecting technological infrastructure from space weather hazards.

ACKNOWLEDGMENTS

This work was supported by the Natural Science Foundation of Shandong Province (Grant No. ZR2024MA046, ZR2021LLZ004) and the Fundamental Research Funds for the Central Universities (Grant No. 202364008). We thank the NMDB database (<http://www.nmdb.eu>), founded under the European Union’s Seventh Framework Programme (FP7, Grant Agreement No. 213007), and the Principal Investigators of the neutron monitors: Tsumeb (Max Planck Institute for Aeronomy), Potchefstroom (North-West University, South Africa), Jungfraujoch (University of Bern, Switzer-

land), Kerguelen (Observatoire de Paris and Institut Polaire Français Paul-Émile Victor), Oulu (Sodankylä Geophysical Observatory, University of Oulu, Finland), Thule (Bartol Research Institute, University of Delaware, USA), and South Pole (University of Wisconsin–River Falls, USA).

AUTHOR CONTRIBUTIONS

Haoyang Li and Zongyuan Ge contributed equally to this work and share co-first authorship. Z.G. conceived the original idea and research concept. H.L. performed the data analysis and numerical experiments. Z.G. and H.L. jointly wrote the initial draft of the manuscript. Z.W. supervised the project, provided critical guidance throughout the research, and revised the manuscript.

REFERENCES

Al Shidi, Q., Pulkkinen, T., Toth, G., et al. 2022, Space Weather, 20, e2022SW003049, doi: [10.1029/2022SW003049](https://doi.org/10.1029/2022SW003049)

Bala, R., & Reiff, P. 2012, Space Weather, 10, S06001, doi: [10.1029/2011SW000737](https://doi.org/10.1029/2011SW000737)

Bell, A. R. 1978, Monthly Notices of the Royal Astronomical Society, 182, 147, doi: [10.1093/mnras/182.2.147](https://doi.org/10.1093/mnras/182.2.147)

Belov, A. V., Dorman, L. I., Eroshenko, E. A., et al. 1995, Nuclear Physics B - Proceedings Supplements, 39A, 136, doi: [10.1016/0920-5632\(95\)80031-9](https://doi.org/10.1016/0920-5632(95)80031-9)

Belov, A. V., Eroshenko, E. A., Oleneva, V. A., & Yanke, V. G. 2015, Journal of Atmospheric and Solar-Terrestrial Physics, 129, 78, doi: [10.1016/j.jastp.2015.04.011](https://doi.org/10.1016/j.jastp.2015.04.011)

Bieber, J. W., Cane, H., Evenson, P., Pyle, R., & Richardson, I. 1999, in AIP Conference Proceedings, Vol. 471, Solar Wind Nine, 137–140, doi: [10.1063/1.58784](https://doi.org/10.1063/1.58784)

Bieber, J. W., & Evenson, P. 1998, Geophysical Research Letters, 25, 2955, doi: [10.1029/98GL02206](https://doi.org/10.1029/98GL02206)

Borovsky, J. E., & Birn, J. 2014, Journal of Geophysical Research: Space Physics, 119, 751, doi: [10.1002/2013JA019193](https://doi.org/10.1002/2013JA019193)

Cane, H. V. 2000, Space Science Reviews, 93, 55, doi: [10.1023/A:1026532125747](https://doi.org/10.1023/A:1026532125747)

Chen, H., Toth, G., Chen, Y., et al. 2025, Space Weather, 23, e2024SW004301, doi: [10.1029/2024SW004301](https://doi.org/10.1029/2024SW004301)

Clem, J. M., & Dorman, L. I. 2000, Space Science Reviews, 93, 335, doi: [10.1023/A:1026508915269](https://doi.org/10.1023/A:1026508915269)

Duggal, S. P., & Pomerantz, M. A. 1976, *Journal of Geophysical Research*, 81, 5032, doi: [10.1029/JA081i028p05032](https://doi.org/10.1029/JA081i028p05032)

Dumbović, M., Vršnak, B., Čalogović, J., & Karlica, M. 2012, *Astronomy & Astrophysics*, 538, A28, doi: [10.1051/0004-6361/201117710](https://doi.org/10.1051/0004-6361/201117710)

Erlykin, A. D., & Wolfendale, A. W. 2006, arXiv e-prints, astro-ph/0601290, doi: [10.48550/arXiv.astro-ph/0601290](https://doi.org/10.48550/arXiv.astro-ph/0601290)

Forbush, S. E. 1938, *Physical Review*, 54, 975, doi: [10.1103/PhysRev.54.975](https://doi.org/10.1103/PhysRev.54.975)

Forman, M. A., & Gleeson, L. J. 1975, *Astrophysics and Space Science*, 32, 77, doi: [10.1007/BF00646241](https://doi.org/10.1007/BF00646241)

Gonzalez, W. D., Joselyn, J. A., Kamide, Y., et al. 1994, *Journal of Geophysical Research*, 99, 5771, doi: [10.1029/93JA02867](https://doi.org/10.1029/93JA02867)

Gopalswamy, N., Lara, A., Yashiro, S., Kaiser, M. L., & Howard, R. A. 2001, *Journal of Geophysical Research*, 106, 29207, doi: [10.1029/2001JA000177](https://doi.org/10.1029/2001JA000177)

Grigoryev, V. G., Starodubtsev, S. A., & Gololobov, P. Y. 2017, *Bulletin of the Russian Academy of Sciences: Physics*, 81, 200, doi: [10.3103/S1062873817020135](https://doi.org/10.3103/S1062873817020135)

Hörandel, J. R. 2006, *Advances in Space Research*, 36, 2357, doi: [10.1016/j.asr.2005.04.001](https://doi.org/10.1016/j.asr.2005.04.001)

Idosa, C., Giri, A., Adhikari, B., Mosisa, E., & Gashu, C. 2023, *Physics of Plasmas*, 30, 083901, doi: [10.1063/5.0157553](https://doi.org/10.1063/5.0157553)

Manoharan, P. K., Gopalswamy, N., Yashiro, S., et al. 2004, *Journal of Geophysical Research*, 109, A06109, doi: [10.1029/2003JA010300](https://doi.org/10.1029/2003JA010300)

Mishra, R. K., & Agarwal, R. 2008, *Brazilian Journal of Physics*, 38, 569, doi: [10.1590/S0103-97332008000400012](https://doi.org/10.1590/S0103-97332008000400012)

Munakata, K., Kuwabara, T., Bieber, J. W., et al. 2005, *Advances in Space Research*, 36, 2357, doi: [10.1016/j.asr.2004.09.006](https://doi.org/10.1016/j.asr.2004.09.006)

Pedersen, M. N., Juusola, L., Vanhamäki, H., Aikio, A. T., & Viljanen, A. 2024, *Journal of Geophysical Research: Space Physics*, 129, e2024JA032656, doi: [10.1029/2024JA032656](https://doi.org/10.1029/2024JA032656)

Richardson, I. G. 2004, *Space Science Reviews*, 111, 267, doi: [10.1023/B:SPAC.0000032689.52830.3e](https://doi.org/10.1023/B:SPAC.0000032689.52830.3e)

Richardson, I. G. 2018, *Living Reviews in Solar Physics*, 15, 1, doi: [10.1007/s41116-017-0011-z](https://doi.org/10.1007/s41116-017-0011-z)

Richardson, I. G., & Cane, H. V. 2010, *Solar Physics*, 264, 189, doi: [10.1007/s11207-010-9568-6](https://doi.org/10.1007/s11207-010-9568-6)

Schlickeiser, R., Oppotsch, J., Zhang, M., & Pogorelov, N. V. 2019, *The Astrophysical Journal*, 879, 29, doi: [10.3847/1538-4357/ab20cc](https://doi.org/10.3847/1538-4357/ab20cc)

Schwenn, R., Raymond, J. C., Alexander, D., et al. 2006, *Space Science Reviews*, 123, 127, doi: [10.1007/s11214-006-9016-y](https://doi.org/10.1007/s11214-006-9016-y)

Singh, T., Hegde, D. V., Kim, T. K., & Pogorelov, N. V. 2025, *The Astrophysical Journal*, 981, 53, doi: [10.3847/1538-4357/ad3a5c](https://doi.org/10.3847/1538-4357/ad3a5c)

Temerin, M., & Li, X. 2002, *Journal of Geophysical Research: Space Physics*, 107, 1472, doi: [10.1029/2001JA007532](https://doi.org/10.1029/2001JA007532)

Tsurutani, B. T., Gonzalez, W. D., Gonzalez, A. L. C., et al. 1995, *Journal of Geophysical Research*, 100, 21717, doi: [10.1029/95JA01476](https://doi.org/10.1029/95JA01476)

Uga, C. I., & Adhikari, B. 2023, *Cosmic Research*, 61, 364, doi: [10.1134/s0010952523600026](https://doi.org/10.1134/s0010952523600026)

Uga, C. I., Goshu, C. Y., & Rikitu, K. S. 2025, *Radio Science*, 60, e2025RS008233, doi: [10.1029/2025RS008233](https://doi.org/10.1029/2025RS008233)

Upendran, V., Tigas, P., Ferdousi, B., et al. 2022, *Space Weather*, 20, e2022SW003045, doi: [10.1029/2022SW003045](https://doi.org/10.1029/2022SW003045)

Vršnak, B., Temmer, M., & Veronig, A. M. 2007, *Solar Physics*, 240, 315, doi: [10.1007/s11207-007-0285-8](https://doi.org/10.1007/s11207-007-0285-8)

Vršnak, B., Žic, T., Vrbanec, D., et al. 2013, *Solar Physics*, 285, 295, doi: [10.1007/s11207-012-0035-4](https://doi.org/10.1007/s11207-012-0035-4)

Zhang, J., Richardson, I. G., Webb, D. F., et al. 2007, *Journal of Geophysical Research*, 112, A10102, doi: [10.1029/2007JA012321](https://doi.org/10.1029/2007JA012321)

Zhu, X. L., Xue, B. S., Cheng, G. S., & Cang, Z. Y. 2015, *Chinese Journal of Geophysics*, 58, 2242, doi: [10.6038/cjg20150704](https://doi.org/10.6038/cjg20150704)